Supplementary Information

Visually Precise, Low-damage, Single-cell Spatial Manipulation with Single-Pixel Resolution

Qi Zhang, Yunlong Shao, Boye Li, Yuanyuan Wu, Jingying Dong, Dongtang Zhang, Yanan Wang, Yong Yan, Xiayan Wang, Qiaosheng Pu* and Guangsheng Guo**

Table of Contents

Supplementary Methods.

Sample preparation. PSF determination: Two microliters of a solution containing yellow-green 100 nm fluorescent beads (Invitrogen, Cat. # F8803) was diluted with 4 mL ultrapure water and uniformly mixed. Fifty microliters of the solution were deposited on the coverslip, the surface of which was coated with polylysine diluted 10 times with ultrapure water (Solarbio, P2100-10), and allowed to sit for 10 min. The coverslip was washed three times with ultrapure water to remove excess beads. Then the sample chamber was made by coverslip and severed cover glass, and the ultrapure water was added to fill the sample chamber for observation.

Silica gel: Silica gel powders were obtained from chromatographic packing material (Haiyang,100-200 mesh), for which the particle size was undefined and the morphology was irregular and nontransparent.

A549 cell suspension: The A549 cell (National Laboratory Cell Resource Sharing Service Platform) culture flask with the culture medium (DMEM, 10% FBS, 1% PS) (Gibco) was removed from the incubator (temperature 37 ℃ and 5% CO2). A pipette was used to remove the culture medium, then 2 mL of PBS buffer was added to rinse the wall, and the PBS buffer was discarded. Next, 500 μL trypsin-EDTA (Gibco) was added to the culture flask, which was placed in the incubator for 2 min, then 2 mL of culture medium was added to stop digestion. The cells were air-blown using a pipette to suspend the cells and then centrifuged at 1200 rpm for 3 min at room temperature. The supernatant was discarded, and 3 mL of the same medium was added. The cells were blown repeatedly to suspend them evenly, and the tube was removed from the cleanroom. The sample chamber was filled with a culture medium containing cells and observed. Polylysine was on the cover glass for 30 min to fix cells.

Nuclear labeling: Thirty microliters of Hoechst 33342 (1 mg/mL; Yeasen Biotech) was added to a centrifuge tube containing 3 mL of culture medium containing cells prepared for observation. The centrifuge tube was placed in an incubator for 30 min then centrifuged at 1200 rpm for 3 min. Then, the supernatant was discarded, three milliliters of PBS buffer was added, the cells centrifuged again at 1200 rpm for 3 min, and the PBS buffer was discarded. Three milliliters of culture medium were added, and the mixture was blown and shaken repeatedly and then observed to prove the existence of trinuclear cells and locate the target. Cell viability verification through trypan blue (Invitrogen, 15250061), the volume ratio of raw trypan blue to cell medium is 1:9. 100 μmol fluorescein disodium salt (Acros Organics) was used for microinjection by the pico pump (Wpi, PV830) to verify the success of penetration.

Tip of capillary: Capillaries (50 μm id, 360 μm od) were produced by Yongnian Ruifeng Chromatographic Device Co., Ltd (Hebei, China), and were pulled to nanopipettes for micromanipulation by a capillary puller (Sutter, P2000).

Aberration-corrected sample chamber: This chamber was made up of the two severed cover glass and integral cover glass, then fixed by glue (Gleihow, 302). The cover glass was customized by ultra-thin glass sheet with a thickness of 100 ± 5 μm, Sample chamber size for PSF determination: L=1.85 mm, L1=0.2 mm, and L2=6 mm. Sample chamber size for all other experiments: L=1.4 mm, L1=0.2 mm, and L2=6 mm (Fig. S3).

Instrument setup. The instrument setup we established was placed on an active isolation workstation (Newport, M-GW3648-PG4-H) except the computer and the controller of the displacement table. The custom body included an inverted microscope system frame (Asi, RAMM-FRAME), a bottom illuminator (Asi, MIM-INV-II-Ex), a high-precision XYZ electric stage (Asi, XYZF stage and controller), and a lens adapter (Asi, COUND-LLG). A customized sample adapter was installed on the electric XY console in order to place the aberration correction sample chamber. The upper two optical paths were perpendicular to each other, and each optical path had an angle of 45° with the horizontal plane[1]. The lens was fixed on the objective turntable (repetitive positioning accuracy ±2.5 μm; Thorlabs, OT1). The turntable was fixed on the lens cone, which was equipped with a slider (Asi, C60-SLIDE-4 S4) and a c-mount (Asi, C60-SLDR-C-MOUNT) to convert the fluorescence mode and to connect to the camera. The lens cone was fixed to a one-dimensional electric displacement platform (Newport, UMR8.25), including an electric actuator (Newport, LTA-HL) and a controller (Newport, XPS-D8), which had sufficient axial load capacity of up to 80 N and provided axial movement at minimum increments of 50 nm. For the inclined objectives, the electric displacement platform was fixed to another displacement platform (DHC, GCM-TPS25MR), which provided y displacement. The y displacement platform was fixed to a 45° angle aluminum alloy bracket with a slider for x displacement, and the bracket was bolted onto the RAMM. The micromanipulation system included a 3D electric nanomanipulator (Smaract, SLC-1730, SLC-2445), a controller (Smaract, MCS-3H) that was fixed to a 3D electric microdisplacement table (Newport, UTS50, UTS100), and a controller (Newport, XPS-D8) that controlled the precise movement of the capillary tip, with a minimum displacement increment of 1 nm. Angular displacement table (Zolix, PSAG15-130) controlled the angle of puncture was fixed to microdisplacement table. The 3D electric microdisplacement table was fixed to the isolation workstation.

Lighting system and optical components. The upper lighting system included a light source with a 5.6×3.0×0.9

mm small-volume surface-mounted device LED (Hgonlly, 26645747969) and a polycarbonate diffusion sheet (Lingmei, LM11) for uniform illumination. Two light-coupling sources (Shibuya, LFP-10WP) supplied coaxial reflection light and helped focus the triple view.

The lower lighting system included a rigid optical fiber bundle (Thorlabs, OSL2YFB) for adjusting the lighting position, which was connected to a halogen light source (Thorlabs, OSL2). A collimation tube (Thorlabs, OSL2COL) containing a planoconvex lens (Thorlabs, LA1289) was used to collimate the beam from the fiber bundle. A bandpass filter (Thorlabs, FGB39) was applied to the narrowband spectrum to reduce the scattering of light, and a polycarbonate scattering sheet (Lingmei, LM11) uniformly dispersed the light. A dichroic mirror (Asi, C60-RA 2nd Port Dichroic Slider) was used to switch the light source at the bottom of the RAMM. The light source (CoolLED, PE-100) provided the coaxial reflection light and enabled the coarse and fine focusing of the triple view through both the luminescent spot on each axis in the visualization and the reflection spot in the camera view. Another light source (CoolLED, PE-300) transmitted excitation light through a multimode optical fiber for fluorescence imaging.

In order to determine imaging under uniform transmission light. we consider the propagation of light through the sample chamber. For the aberration-corrected sample chamber, according to the independent propagation of light law, the refraction of light law and the characteristics of light passing through a parallel plate in geometric optics:

$$n_1 \sin I = n_2 \sin I' \qquad (1)$$

where n_1 and n_2 are the refractive indexes of media 1 and 2, I is the angle between the incident light and the normal, and I' is the angle between refracted light and the normal.

The incident angle I is approximately 70.1°for uniform coaxial transmission illumination. surface tension causes droplets added to the chamber to quickly occupy the whole sample chamber. The sample chamber does not leak, and the volume of liquid remains stable. Because of capillary action, any evaporating liquid will be continuously supplemented by the liquid at both ends to form a dynamic balance.

In the upper two optical paths, a bandpass filter (Thorlabs, MF530-43) was used to determine the PSF. In the bottom optical path, the fluorescence of the nucleus was observed using filter sets (Nikon, MBE49100), and the PSF was determined using filter sets (Nikon, MBE44725).

Detection and acquisition system. Detection system: The long working distance objectives included three 20× objectives (working distance, WD=13 mm, NA=0.4; Nikon, MUE21200), two 100× objectives (WD=10 mm,

NA=0.6; Nikon, MUE31900) for the two upper optical paths, and 100× objectives (WD=4.5 mm, NA=0.8; Nikon, MUE21900) for the bottom optical path to eliminate the space limitation between objectives. According to Nikon's objective lens manual, fluorescence imaging in the visible band is applicable. The lens cone (Mitutoyo, VMU-H) contained a dichroic beam split and an aperture stop, which was used to complete the beam propagation and focus the multiple views.

Acquisition system: The upper two optical paths used scientific complementary metal-oxide semiconductor (sCMOS) cameras (PCO, panda), which had a 16-bit pixel depth, and 2048×2048 pixels with a size of 6.5 μm that coordinated with the 100× objectives. The imaging resolution was 6.5 μm /100 = 65 nm. The main parameters of the bottom sCMOS camera (Hamamatsu, ORCA-FLASH4.0 LT PLUS) were the same as those of the upper camera.

The upper two optical paths included the objectives and a 1× lens, which produced an upright image. The bottom optical path had an added right-angle prism mirror (Asi, c60-cube-25mmBS), which produced an inverted image (Fig. S6).

STSRM system positioning principle. The positioning principle is essentially the spatial positioning between the centroid points, which is suitable for approximate central symmetry, the schematic diagram of the principle applies for spatial location is as follows:

From the relation between xyz and lmn coordinates :

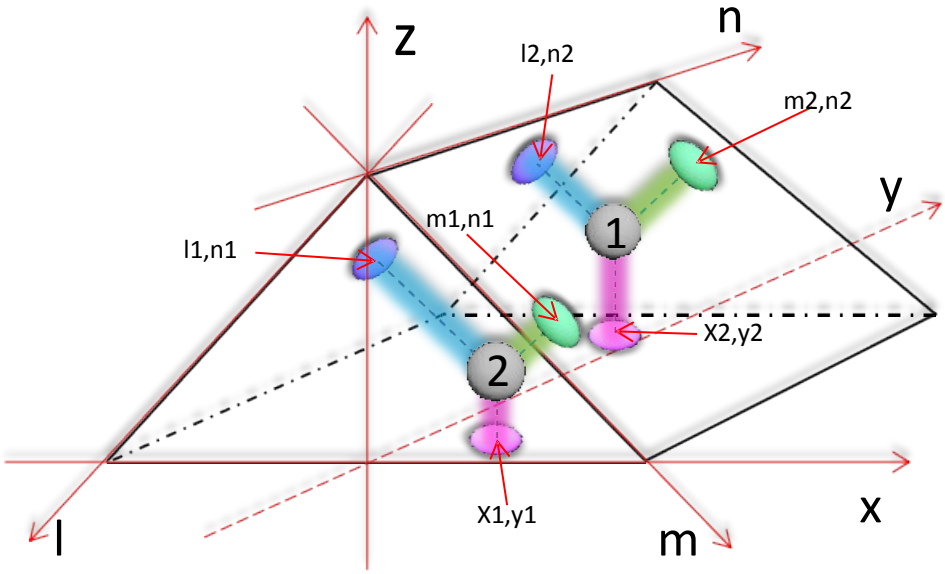

Assume 1 and 2 are two spheres (centrosymmetry) in space, the radius is R1 and R2 respectively, and other coordinates are the centroid of each projection plane

$$(l_2-l_1)^2+(n_2-n_1)^2+(m_2-m_1)^2 = (x_2-x_1)^2+(y_2-y_1)^2+(z_2-z_1)^2 \qquad (2)$$

Ideally, if 1 and 2 are spheres and symmetric around the center, $\Delta_1(n_2-n_1)=\Delta_2(n_2-n_1)=\Delta(y_2-y_1)$ in *ln, mn,* and *xy* plane, Δz would be calculated. In fact, a centroid positioning error (Er) can occur including non-centrosymmetric shape and measurement, define $Er=\max(|\Delta_1(n_2-n_1)-\Delta_2(n_2-n_1)|, |\Delta_1(n_2-n_1)-\Delta(y_2-y_1)|, |\Delta_2(n_2-n_1)-\Delta(y_2-y_1)|)$, and we take the average $\Delta z=(\Delta z_1+\Delta z_2)/2$. the results of spatial position simulation obtained by calculation can be verified by experiments.

Cone angle correction. When the pipette was imaged[2], the tilt angle relative to the optical axis was defined α. Because of the tilt, the angle that was measured in the optical image, ϕ, was not the same as the true cone angle in the scanning electron microscope, θ. the relationship between the measured angle, the cone angle, and the tilt angle could be obtained by equation：

$$\cos\varphi = \frac{\cos^2(\frac{\theta}{2})\sin^2(\alpha) - sin^2(\frac{\theta}{2})}{\cos^2(\frac{\theta}{2})\sin^2(\alpha) + sin^2(\frac{\theta}{2})} \qquad (3)$$

Software control and data processing. A micromanager 1.4.22 was used to connect the electric XYZ stage, the bottom LED light source Ls5. (Fig. S6), and all cameras. Bioimaging1.0 was used to control triple-view imaging, deconvolution of the triple-view fluorescent series of images in real-time was based on the Wiener filter algorithm. Zemax 2016 was used to simulate optical experiments of different imaging modes. Programs were written with LabVIEW 2017 to both control experimental displacements and obtain the coordinates of the spatial points. Images were processed using the software Fiji[3] 1.52n. 3ds Max2015 was used to simulate the 3D multiview dynamic processes of cells and obtain the volume of cytoplasmic damage by Boolean calculation. The 3dsmax could be very compatible with our system because it could supply the same simultaneous triple-view and intuitive steric information. Data plots were created with Origin 2017.

Supplementary Figures

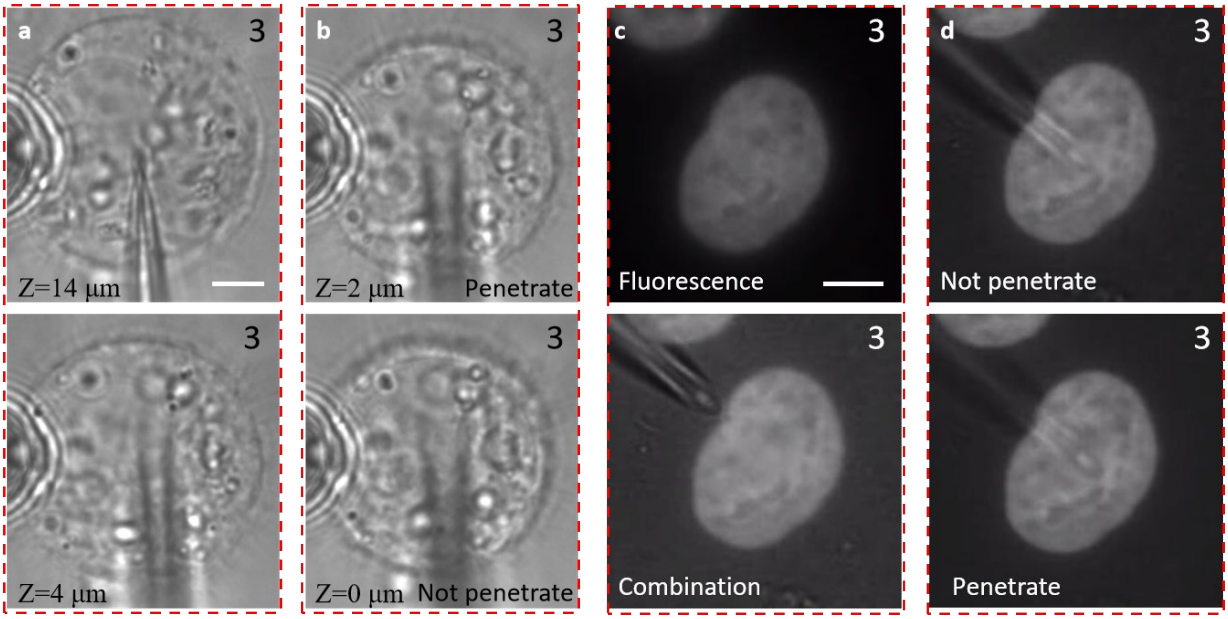

Fig. S1 | Traditional micromanipulation carried on an inverted fluorescence microscope (Ti-E, Nikon) with 100×, numerical aperture (NA) = 1.4 objectives.

From any of a single image, it is impossible to judge the spatial position of the pipette tip relative to the cell (a) and therefore hard to make sure whether the cell was contacted and penetrated (b), Z represents the relative distance of the tip. Micromanipulation combining the bright-field image with the fluorescence image is common (c), but to differentiate the accurate position of the probe tip is still difficult (d). (Scale bar: 5 μm.).

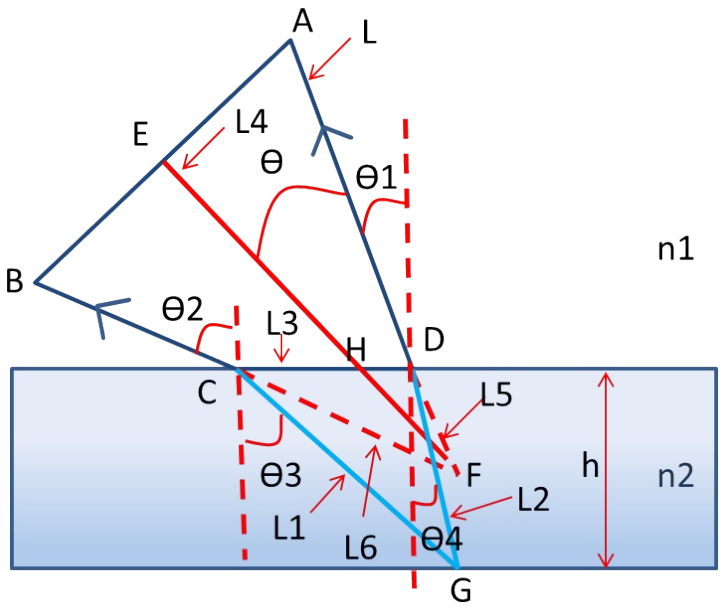

Fig. S2 | Schematic diagram of the light path for imaging underwater objects with tilted 45° lens.

The lens is an ideal coaxial optical system, the height of the flat liquid is *h*, and the wavelength of light is constant.

Define AF=*L*, CG=*L1*, DG=*L2*, CD=*L3*, EF=*L4*, DF=*L5*, CF=*L6*, S1=AG, S2=BG.

According to the condition of perfect imaging: equal optical path principle. If the object is perfectly imaged on the optical axis, it should be:

$$\Delta S = S_2 - S_1 = \int_G^B ndl - \int_G^A ndl = 0$$

$$S_1 = \int_G^D n2dl + \int_D^A n1dl$$

$$S_2 = \int_G^C n2dl + \int_C^B n1dl$$

Calculated: $\Delta S = S_2 - S_1 = hn_2(1/\cos\Theta_3 - 1/\cos\Theta_4) + hn_1(\sin(\Pi/2-\Theta_2) - \sin(\Pi/2+\Theta_1))\sin(\Theta_3-\Theta_4)/\cos\Theta_3 \sin 2\Theta \sin(\Pi/2+\Theta_4)$;

$\Theta_2 = \Pi/4+\Theta$, $\Theta_1 = \Pi/4-\Theta$, $n_1\sin\Theta_2 = n_2\sin\Theta_3$, $n_1\sin\Theta_1 = n_2\sin\Theta_4$;

$\Delta S = |f(\Theta, n_1, n_2, h)| \neq 0$, and Θ， n_1， n_2 are known, $\Delta s = |f(h)|$, the smaller the *h*, the better the imaging.

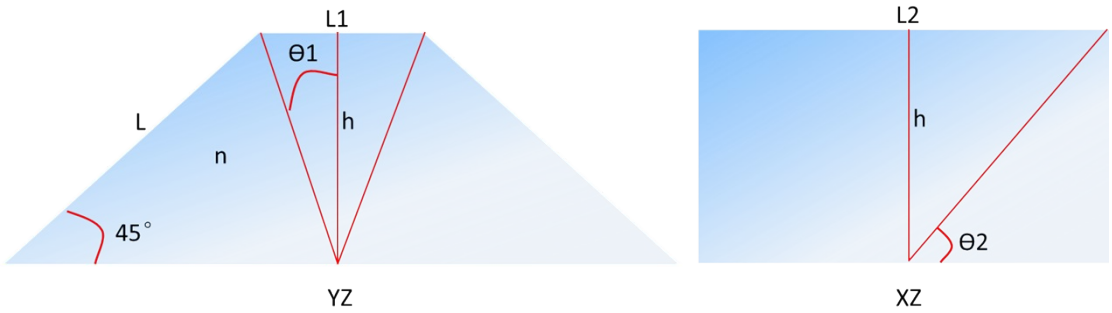

Fig. S3| shape of aberration correction sample chamber.

The device is composed of glass sheets so that the optical path from any object point to the image point is equal. The customized ultra-thin cover glass sheet 100 ± 5 μm is used to reduce the aberration for imaging. $L1=2h\tan\Theta_1$. $h=L/\sqrt{2}=L2\tan\Theta_2/2$

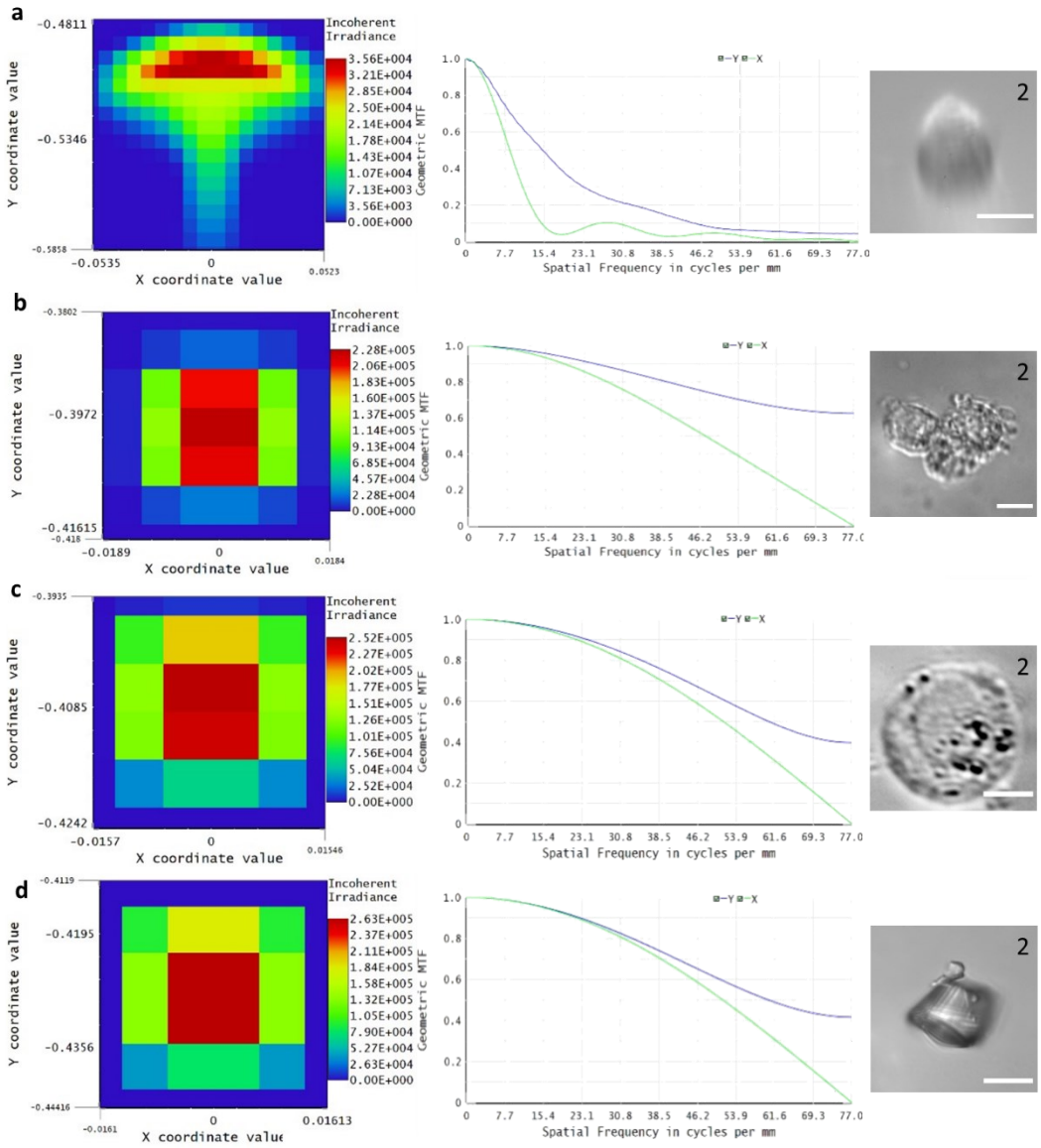

Fig. S4 | False-color image of light distribution, MTF curve, and experimental image of the cell corresponding to the different imaging modes in tilt view.

Optical simulation by the paraxial lens and point source in the non-sequential mode. (a) The distribution (imaging) results of light (A549 cells) in higher liquids level (1mm). (b) The distribution (imaging) results of light (A549 cells) in the lower liquid (The simulative liquid level is 0.1 mm, the experimental liquid level is about 70 μm). (c) Distribution (imaging) results of light (A549 cells) in the sample chamber. (d) The distribution (imaging) results of light (Silica gel) in the air. (Scale bar: 10 μm)。

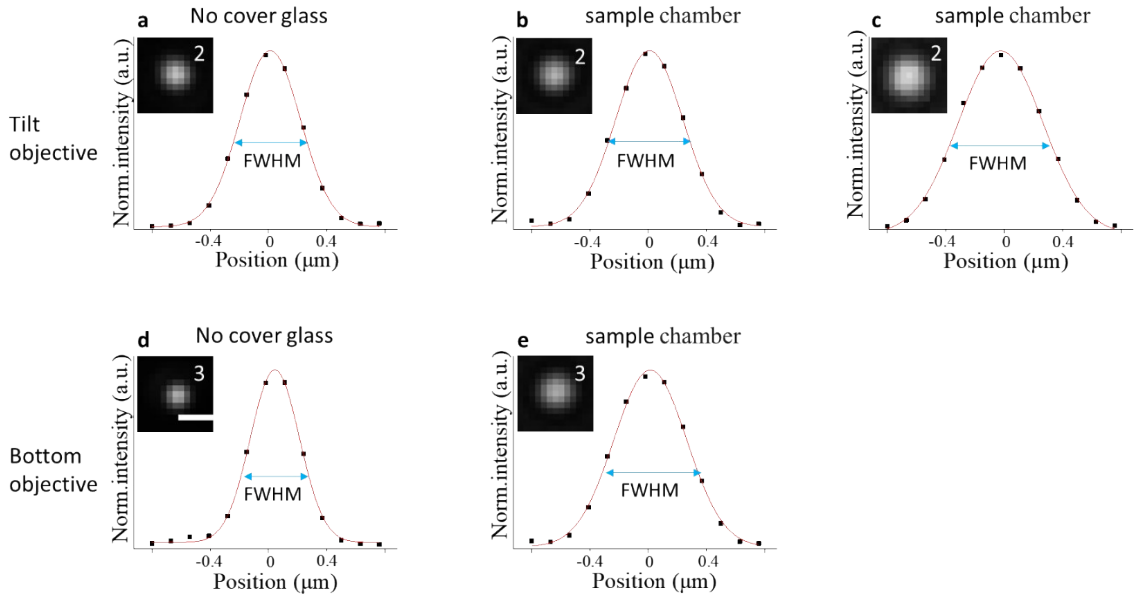

Fig. S5 | Detection of PSF in different modes.

Oblique objectives: (a) Without cover glass, the resolution: 525 ± 11 nm (n=9 beads). (b) The fluorescent beads were close to the inner wall of the sample chamber (distance between the oblique cover glass and beads was about 0 mm), the resolution: 527 ± 9 nm (n=8 beads). (c) The fluorescent beads were in the center bottom of the sample chamber (distance between the oblique cover glass and beads was about 1mm), the resolution: 669 ± 23 nm (n=8 beads). Bottom objectives: (d) Without cover glass, the resolution:432 ± 15 nm (n=9 beads). (e) The fluorescent beads were close to the inner wall of the sample chamber (distance between the bottom cover glass and beads was about 0 mm), the resolution: 542 ± 14 nm (n=10 beads). The thickness of glass was 100 μm, objective 3 decreased by about 110 nm resolution and objective 1, 2 were not unaffected, and distance was 1mm, objective 1, 2 decreased by about 140 nm resolution while the difficulty of manipulation would increase. (Scale bar: 1 μm.)

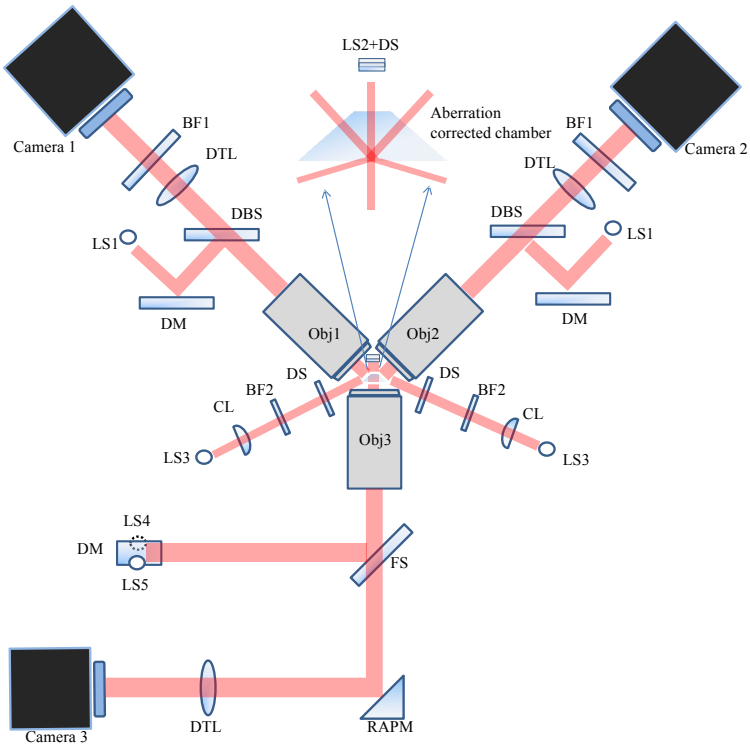

Fig. S6 | The optical design of STSRM system.

Simultaneously triple-view imaging in bright field. Bottom view imaging: The light of the power controllable SMD LED (Ls2) passes through the diffuse scatterer (DS), The sample, objective 3, right-angle prism mirror(RAPM) and detection tube lenses (DTL) reach Camera3. Left upper view imaging: Light from the halogen lamp (LS3) passes through the collimating lens (CL), a band-pass filter (BF), diffuse scatterer (DS), sample, objectives 1, a dichroic beam splitter (DBS) and detection tube lens (DTL) to Camera1. The right upper lighting and imaging system are the same as the left upper optical path, and structures are symmetrical.

Triple-view reflective imaging and focus. Bottom view imaging: light from the LED (ls5) passes through aperture stop, dichroic mirror (DM), a dichroic beam splitter (filter sets) (FS), objective 3, sample, right-angle prism mirror (RAPM), and detection tube lens (DTL) to Camera3. Left upper view imaging: Light from optical fiber coupling light source (LS1) passes through the aperture stop, dichroic mirror (DM), a dichroic beam splitter (DBS), objective lens 1, sample and detection tube lenses (DTL) to Camera1. By adjusting the aperture stop, first, align the three light path reflection spot roughly, then find out the position of the bottom reflection spot from the three-camera field of view and align precisely.

Simultaneously triple-view imaging in fluorescence mode: The light source (Ls4) passes through a multimode optical fiber, dichroic mirror (DM), filter sets (FS), and objective 3 to reach the sample, and the stimulated emission light reaches each camera along with each objective, filter sets (FS) or band-pass filter (BF1), respectively.

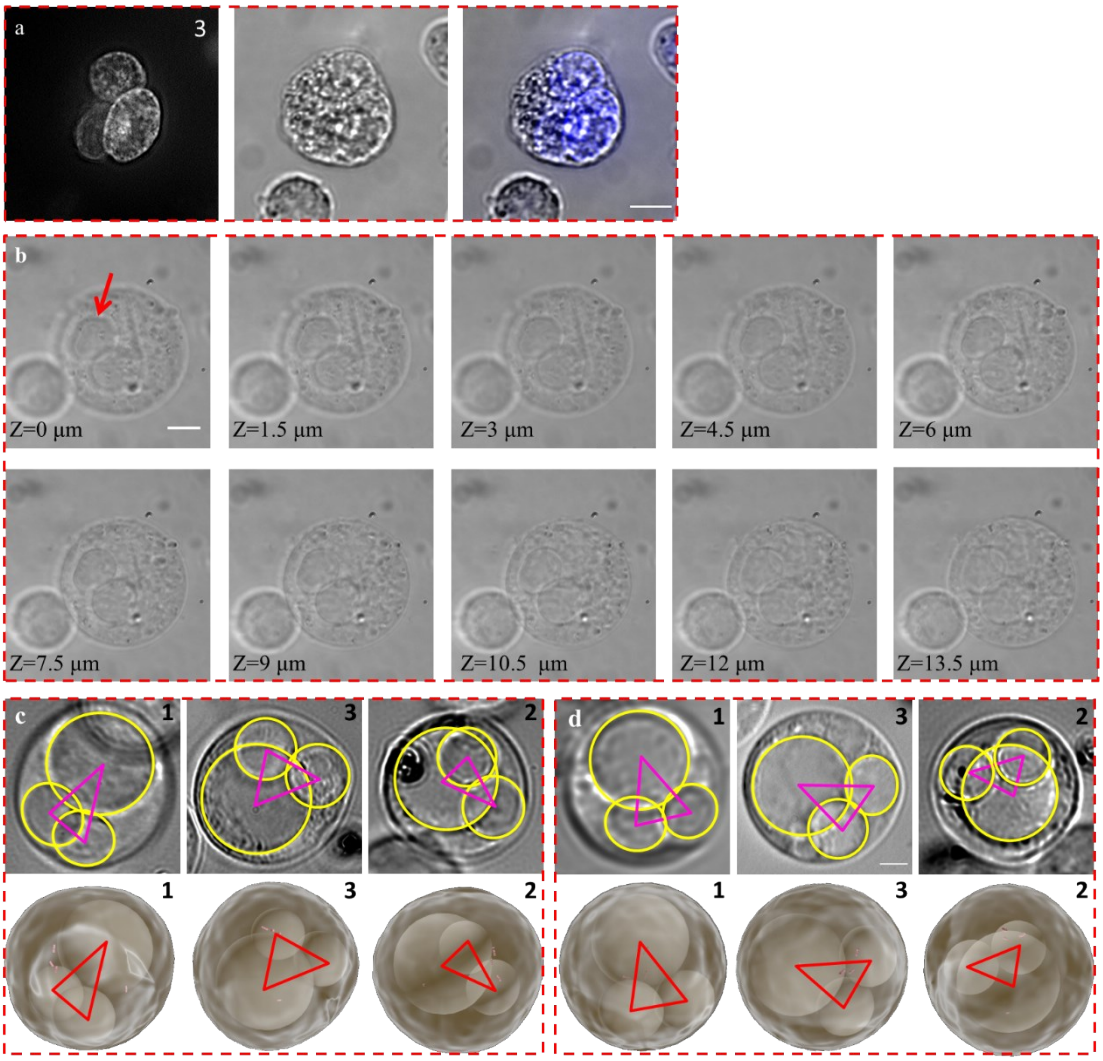

Fig. S7 | A549 multinucleated giant cells in the bottom view and triple-view.

(a) Cell nuclei were labeled with hoechst33342 (blue), cells in the bright field, and channels merge to prove the existence of multinucleated giant cells. (Scale bar, 5 μm.) (b) It was very difficult to distinguish the spatial position between cells and nuclei (red arrow) through our subjective judgment. (Scale bar, 10 μm.) (c) Focused every nucleus, recorded imagings, and fitted contours (yellow circle) in the triple views by Fiji, connected centroids (magenta triangle) of the three nuclei in the experiment (Er <1 μm), and completed the corresponding simulation (red triangle). (d) Experimental and simulated triple views of cells after the second slight disturbances, when the red triangles are approximately overlaps with the magenta triangles in the triple views, the simulated rotation stops, the rotation accuracy was ±5° obtained by matching red and magenta triangle. (Scale bar, 5 μm.)

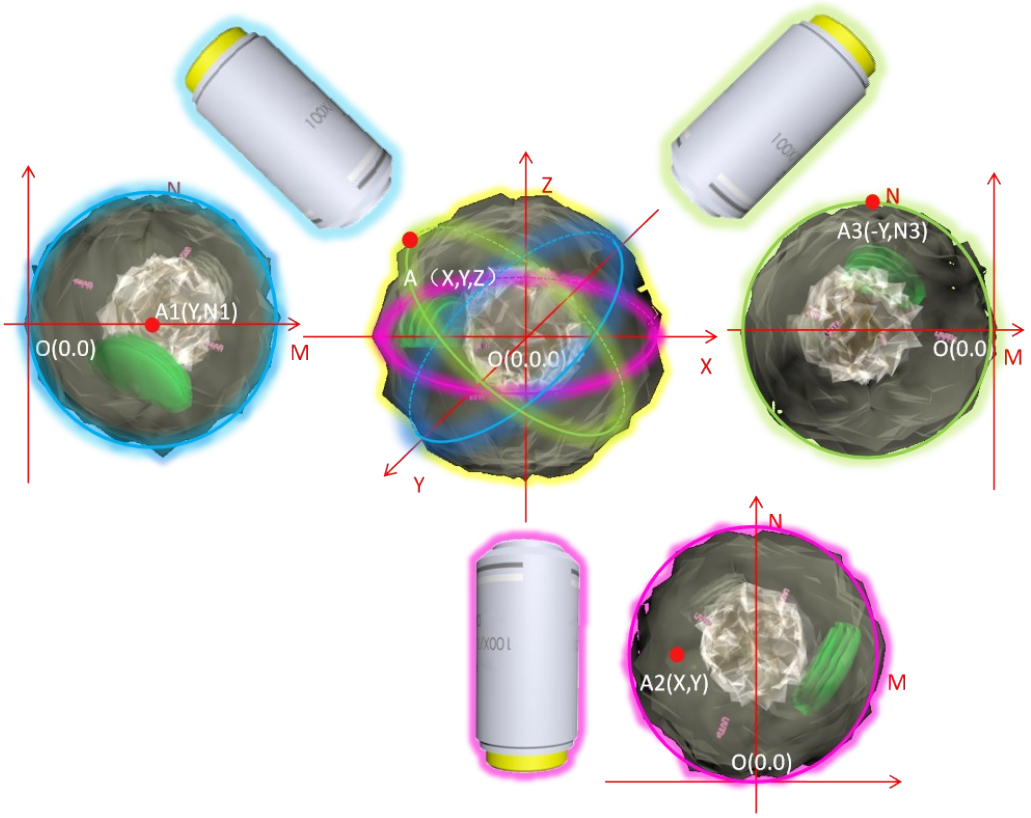

Fig. S8| Coordinate conversion system.

Select a space point as the origin, and convert the 3D coordinates of any point A (x, y, z) to the 2D coordinates of each view. The conversion rules are shown in Table S1.

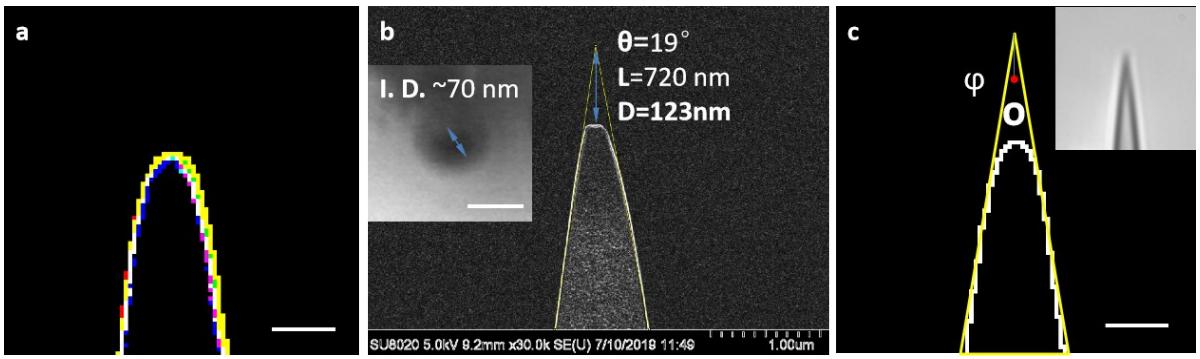

Fig. S9 | Characterization of the microprobe tip under the microscope.

(a) Through Ostu threshold and outline, the contours of the tip acquired from different periods (represented in different colors) were used to evaluate the observation accuracy. (n = 7). (Scale bar: 1 μm.). (b) The angle, θ, diameter, D, of the tip and distance between the tip and the intersection point, L, were determined from the images of the scanning electron microscope (SEM), the I.D. was about 70 nm. (Scale bar: 100 nm.). (c) After correction of θ and L for the tip (α=80°) (See cone angle correction), the central point of the tip O could be determined with an accuracy of < 1 pixel. (Pixel size: 65 nm) (Scale bar: 1 μm.)

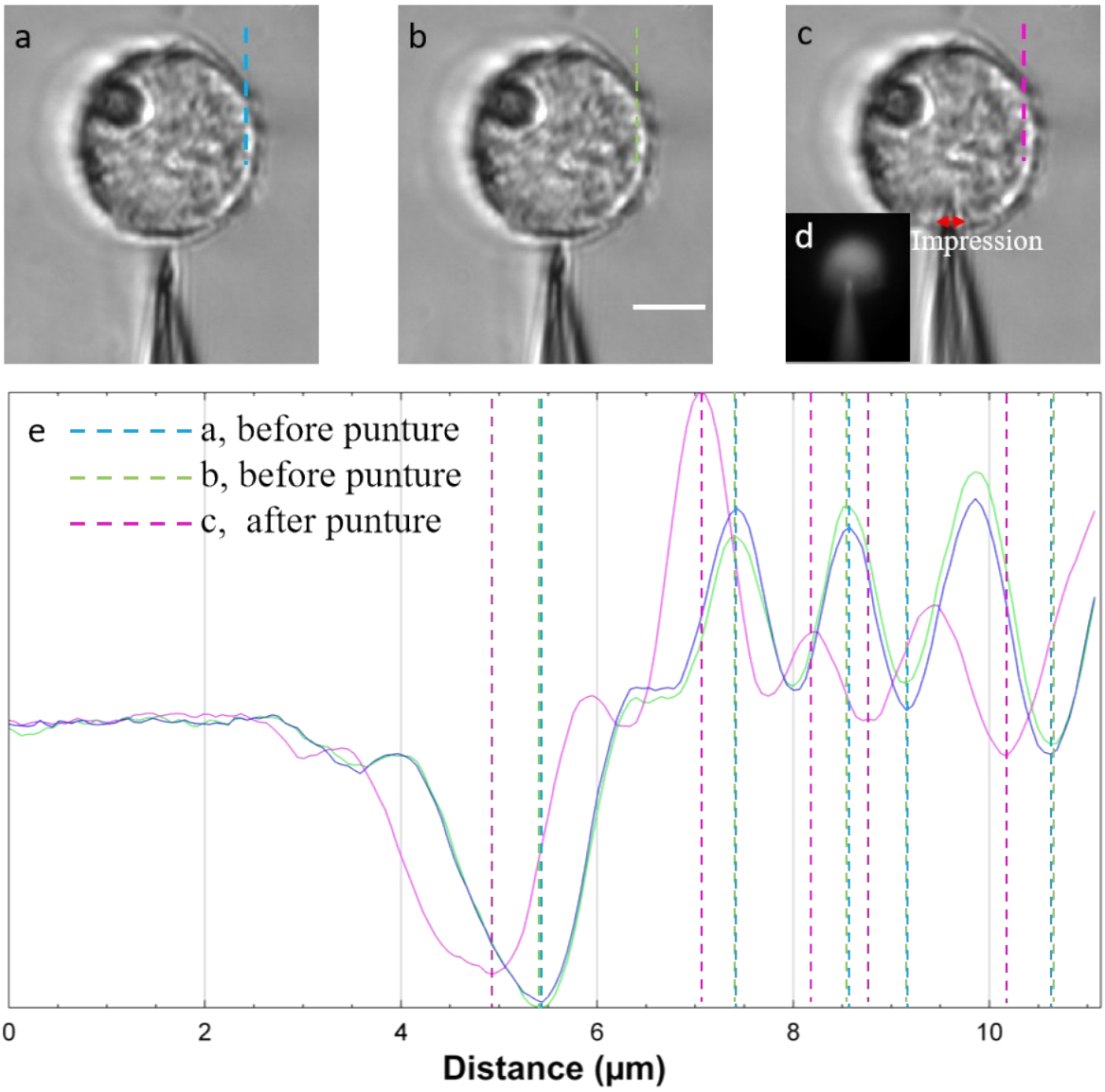

Fig. S10 | Relationship between cell punctured and displacement.

(a), (b) The cell was fixed on cover glass by polylysine. (c) The cell was punctured and successfully injected into the fluorescent dye (fluorescein disodium salt) (d). (e) By blue, green, and pink dot lines, the cell was also fixed stable, and when the displacement was 390~520 nm (6-8 pixels), all cells were punctured (n=7). We find that other parameters of penetration including impression on the cell surface (red arrow, > 1μm) corresponded to Shen *etal* work used a 150 nm quartz tip (~400 nm).[4] (Scale bar: 5 μm.)

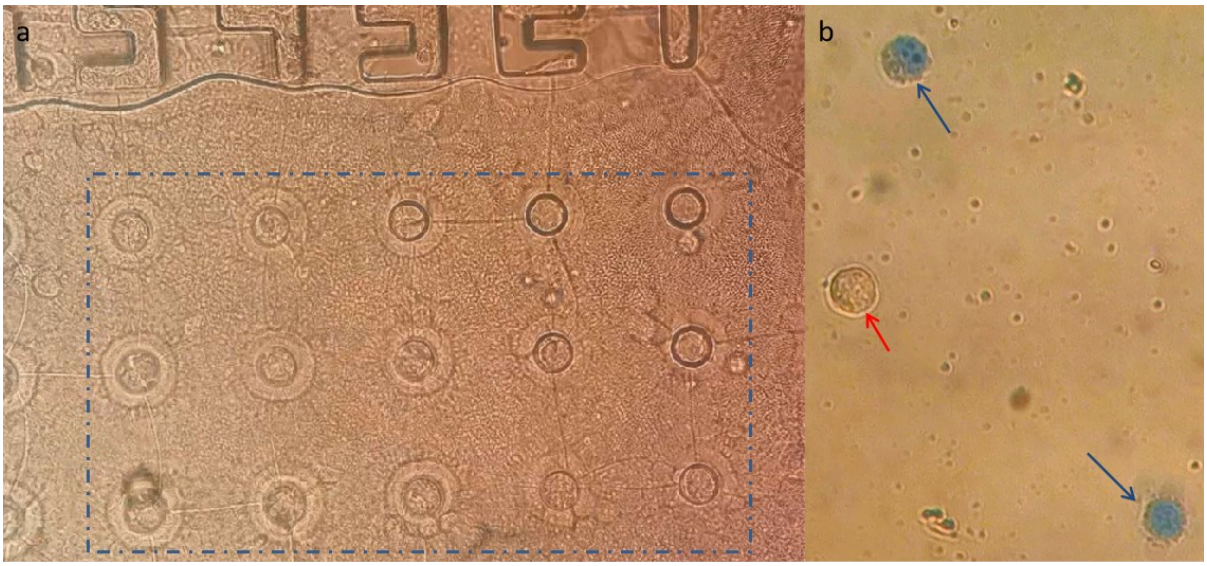

Fig. S11 | Cell viability verification

(a) 15 punctured cells in micropores were still alive verified by trypan blue staining (blue box). (b) Living cell (red arrow) and dead cell (blue arrow) by trypan blue staining.

Supplementary Table

Table S1. The conversion rule

Conditions	N_1	N_3
$0 \le \frac{z}{x} < 1, z \ge 0, x > 0$	$\sqrt{x^2+z^2}\cos(\frac{\pi}{4} - \tan^{-1}\frac{z}{x})$	$-\sqrt{x^2+z^2}\sin(\frac{\pi}{4} - \tan^{-1}\frac{z}{x})$
$1 \le \frac{z}{x} < \infty, z \ge 0, x > 0$	$\sqrt{x^2+z^2}\sin(\frac{3\pi}{4} - \tan^{-1}\frac{z}{x})$	$\sqrt{x^2+z^2}\cos(\frac{3\pi}{4} - \tan^{-1}\frac{z}{x})$
$-1 \le \frac{z}{x} < 0, z > 0, x < 0$	$-\sqrt{x^2+z^2}\sin(\frac{\pi}{4} - \lvert\tan^{-1}\frac{z}{x}\rvert)$	$\sqrt{x^2+z^2}\cos(\frac{\pi}{4} - \lvert\tan^{-1}\frac{z}{x}\rvert)$
$-\infty \le \frac{z}{x} < -1, z > 0, x < 0$	$\sqrt{x^2+z^2}\cos(\frac{3\pi}{4} - \lvert\tan^{-1}\frac{z}{x}\rvert)$	$\sqrt{x^2+z^2}\sin(\frac{3\pi}{4} - \lvert\tan^{-1}\frac{z}{x}\rvert)$
$0 \le \frac{z}{x} < 1, z \le 0, x < 0$	$-\sqrt{x^2+z^2}\cos(\frac{\pi}{4} - \lvert\tan^{-1}\frac{z}{x}\rvert)$	$\sqrt{x^2+z^2}\sin(\frac{\pi}{4} - \lvert\tan^{-1}\frac{z}{x}\rvert)$
$1 \le \frac{z}{x} < \infty, z \le 0, x < 0$	$-\sqrt{x^2+z^2}\sin(\frac{3\pi}{4} - \lvert\tan^{-1}\frac{z}{x}\rvert)$	$-\sqrt{x^2+z^2}\cos(\frac{3\pi}{4} - \lvert\tan^{-1}\frac{z}{x}\rvert)$
$-1 \le \frac{z}{x} < 0, z < 0, x > 0$	$\sqrt{x^2+z^2}\cos(\frac{\pi}{4} + \lvert\tan^{-1}\frac{z}{x}\rvert)$	$-\sqrt{x^2+z^2}\sin(\frac{\pi}{4} + \lvert\tan^{-1}\frac{z}{x}\rvert)$
$-\infty \le \frac{z}{x} < -1, z < 0, x > 0$	$-\sqrt{x^2+z^2}\cos(\frac{3\pi}{4} - \lvert\tan^{-1}\frac{z}{x}\rvert)$	$-\sqrt{x^2+z^2}\sin(\frac{3\pi}{4} - \lvert\tan^{-1}\frac{z}{x}\rvert)$
$x = 0$	$z\cos\frac{\pi}{4}$	$z\sin\frac{\pi}{4}$

Supplementary Movies

Movie S1: The simulation of cells with two times spatial rotations, the simulated results of nuclei were highly consistent with the experimental results.

Movie S2: The simulation of penetrating point A, which was located on the edge of quadrants 2 and 4, not in the cell. The simulation was in good agreement with the experimental results for the tip position relative to the cell.

Supplementary References

1. Y. Wu, P. Wawrzusin, J. Senseney, R. S. Fische8r, R. Christensen, A. Santella, A. G. York, P. W. Winter, C. M. Waterman, Z. Bao, D. A. Colon-Ramos, M. McAuliffe, H. Shroff, *Nat. Biotechnol.* 2013, **31**, 1032-1038.

2. M. A. Stockslager, C. M. Capocasale, G. L. Holst, M. D. Simon, Y. Li, D. J. McGruder, E. B. Rousseau, W. A. Stoy, T. Sulchek, C. R. Forest, *Precis. Eng*. 2016, ***46***, 88-95.

3. J. Schindelin, I. Arganda-Carreras, E. Frise, V. Kaynig, M. Longair, T. Pietzsch, S. Preibisch, C. Rueden, S. Saalfeld, B. Schmid, J. Y. Tinevez, D. J. White, V. Hartenstein, K. Eliceiri, P. Tomancak, A. Cardona, *Nat. Methods* 2012, ***9***, 676-682.

4. Y. J. Shen, M. Nakajima, M. R. Ahmad, T. Fukuda, S. Kojima and M. Homma, *2009 Ieee International Conference on Mechatronics and Automation, Vols 1-7, Conference Proceedings*, 2009, 1849-1854.